Functionalized MoS2 nanosheets enabled nanofiltration membrane with enhanced permeance and fouling resistance

Environmental Technology & Innovation 27 (2022) 102719

Contents lists available at ScienceDirect

Environmental Technology & Innovation

journal homepage: www.elsevier.com/locate/eti

Functionalized MoS_2 nanosheets enabled nanofiltration membrane with enhanced permeance and fouling resistance

Deepak Surendhra Mallya [a,*], Guoliang Yang [b], Weiwei Lei [b], Shobha Muthukumaran [c], Kanagaratnam Baskaran [a]

[a] School of Engineering, Deakin University, Waurn Ponds, Geelong, Victoria 3216, Australia
[b] Institute of Frontier Materials, Deakin University, Waurn Ponds, Geelong, Victoria 3220, Australia
[c] Institute for Sustainable Industries & Liveable Cities, College of Engineering and Science, Victoria University, Melbourne, VIC 8001, Australia

ARTICLE INFO

Article history:
Received 31 March 2022
Received in revised form 19 May 2022
Accepted 31 May 2022
Available online 8 June 2022

Keywords:
Thin film nanocomposite membrane
Organic fouling
Natural organic matter
MoS_2 nanosheets

ABSTRACT

In this study, a novel thin film nanocomposite (TFN) membrane incorporated with -OH functionalized molybdenum disulfide (OH-MoS_2) nanosheets was fabricated through interfacial polymerization between piperazine (PIP) and trimesoyl chloride (TMC) by addition of nanosheets in the aqueous phase. The physicochemical characterizations of the resultant TFN membrane confirmed the embedding of OH-MoS_2 nanosheets and showed excellent compatibility with polypiperazine amide (PPA) matrix, as well as the nanosheets incorporation significantly increased the hydrophilicity, negative charge, surface roughness. In addition, the hydroxyl groups attached to the MoS_2 nanosheets can be covalently bonded into the skin layer through its reaction with TMC, promoting excellent compatibility with the polymer matrix. At an optimum concentration of 0.010 wt% OH-MoS_2, the TFN membrane exhibited 45.17% increase in pure water flux (84.14 L m^{-2} h^{-1}) when compared to control membrane (57.96 L m^{-2} h^{-1}) and maintained stable salt rejection for Na_2SO_4 (96.67%). This optimized TFN membrane exhibited high normalized flux of 96.92% when compared to 91.22% for control membrane and high flux recovery ratio of 98.88% was maintained as well as enhanced organic removal at 89.14% in terms of dissolved organic carbon (DOC) and 99.2% as ultraviolet absorbance at 254 nm (UV_{254}) was recorded during 6 h filtration studies with humic acid containing feed water. 0.010 wt% OH-MoS_2 incorporated membranes exhibited enhanced permeance, salt rejection and stability along with excellent fouling resistance and organic removal demonstrating the potential of OH-MoS_2 nanosheets for engineering high performance and fouling resistant TFN NF membranes for water treatment.

1. Introduction

Providing safe drinking water for human consumption is a major challenge in several developing countries. Fresh surface water from resources such as lakes, rivers and reservoirs contribute majorly for drinking water production in Australia. However, surface water contains a host of natural organic matter (NOM) which needs to be removed prior to the disinfection stage. NOM is a complex mixture of organics derived from the breakdown of terrestrial plants and as by-products of aquatic organisms. Presence of NOM affects the organoleptic properties of the water and contributes to the

* Corresponding author.
E-mail address: dmallya@deakin.edu.au (D.S. Mallya).

https://doi.org/10.1016/j.eti.2022.102719

formation of carcinogenic disinfection by-products (DBP) (Abdikheibari et al., 2018; Metsämuuronen et al., 2014). Water authorities throughout the world recommend the removal of these organics prior to the disinfection stage to reduce the DBP formation in the produced water (WHO, 2011; USEPA, 2006).

Nanofiltration (NF) membranes have been extensively utilized in various applications such as surface water treatment, desalination, and wastewater facilities due to its high contaminant removal properties, minimum consumption of chemicals and low energy requirements when compared to reverse osmosis (RO) membranes (Du et al., 2022). Innovation in NF membrane development supported application for NOM removal to yield high-quality drinking water with minimum disinfectant demand (Abdikheibari et al., 2020; Shurvell et al., 2015). NF membranes are typically fabricated via interfacial polymerization (IP) and reportedly achieved high removal of NOM (75%–95%) (Abdikheibari et al., 2020; Shurvell et al., 2015; Metsämuuronen et al., 2014). For instance, commercial NF membrane (XN 45) achieved removal of 84.17% and 97.66% in terms of dissolved organic carbon (DOC) and ultraviolet absorbance at 254 nm (UV_{254}) respectively (Abdikheibari et al., 2018). The potential of NF membranes to support organic removal was compared to other primary methods such as coagulation, flocculation and hybrid processes utilizing ultrafiltration (UF)/microfiltration (MF) membranes and found to produce drinking water with lower DBP forming potential (Metsämuuronen et al., 2014). For instance, NF membrane removed 650% and 341% more UV_{254} and DOC compared to conventional treatment plant consisting of coagulation and sand filtration (Abdikheibari et al., 2020). NF treated water reported lower chlorine demand at 1.1 mg L^{-1} compared to 2.1 mg L^{-1} for conventionally treated water, which supports in production of healthier drinking water (Abdikheibari et al., 2020). However, NF membranes are prone to organic fouling caused due to the deposition of the organic foulants on the membrane surface. Organic fouling drastically impacts the membrane performance and necessitates frequent chemical cleaning and replacement of membranes leading to increased cost for operation and maintenance (Mansourpanah et al., 2021; Moradi et al., 2021; Alosaimi et al., 2022). In addition, the deposition of organic foulants may trigger biological growth leading to deterioration of membrane structure and performance (Pichardo-Romero et al., 2020; Zhang et al., 2022).

Recent advances in nanoscience facilitates fabrication of fouling resistant membranes by incorporation of nanomaterials such as graphene and its compounds, carbon nanostructures, zeolites, metal and metal oxide etc. during membrane fabrication via IP reaction (Zhao et al., 2021; Du et al., 2022). Emerging 2D nanosheet materials such as graphene oxide (GO) (Kang et al., 2019), boron nitride (BN) (Abdikheibari et al., 2018), molybdenum disulfide (MoS_2) (Li et al., 2019), metal carbides (MXene) (Wang et al., 2020), covalent organic frameworks (COFs) (Lim et al., 2020), graphitic carbon nitride (g-C_3N_4) (Shahabi et al., 2019) and metal organic frameworks (MOFs) (Wen et al., 2019) were added during IP reaction to generate thin film nanocomposite (TFN) membranes, leading to enhanced water permeance and selectivity, as well as high organic fouling resistance. The surface properties of these 2D-enabled TFN membranes, including the wettability, streaming potential, and charge as well as morphology and roughness, may be carefully engineered to impart high organic fouling resistance (Mallya et al., 2021). Among them, MoS_2 nanosheet materials are promising candidates to fabricate 2D enabled TFN membranes due to its properties such as atomic thickness, hydrophilicity, negative charge, stability and its ability to bridge trade-off between flux and salt rejection performance of TFN membranes (Li et al., 2019; Yang and Zhang, 2019; Mallya et al., 2021).

MoS_2 is a typical transition metal chalcogenide, consists of hexagonal layers of Mo and S atoms. MoS_2 is naturally available abundant on earth's crust as molybdenite mineral making it more accessible for scalable production (Ahmadi et al., 2021; Wu et al., 2017). Incorporation of MoS_2 nanosheets improved the hydrophilicity, surface roughness, negative charge and cross-linking degree of the polyamide layer which translated into enhanced water permeance and salt rejection performance of the membranes (Li et al., 2019; Yang and Zhang, 2019; Yang et al., 2020). At an optimum concentration of 0.010 wt%, incorporation of MoS_2, tannic acid modified MoS_2 (TA-MoS_2), tannic acid-Fe^{3+} modified MoS_2 (TA-Fe^{3+} MoS_2) and oxidized MoS_2 (O-MoS_2) in separate studies, resulted in enhancement in water permeance by 129%, 24.36%, 55.10% and 154.34% when compared to the control membranes in respective studies, as well as maintained very high salt rejection > 94% for Na_2SO_4 (Li et al., 2019; Ma et al., 2019; Zhang et al., 2020a; Yang et al., 2020). However, there are problems associated with the scalable nanosheets production and its compatibility with polymers (Li et al., 2019; Ahmadi et al., 2021; Gupta et al., 2015). In addition, there is a lack of detailed studies exploring the NOM removal and fouling resistance performance for MoS_2 incorporated membranes.

In this work, -OH functionalized MoS_2 (OH-MoS_2) nanosheets were incorporated as novel nanofillers into the polypiperazine amide (PPA) skin layer during IP process to improve the organic fouling resistance and compatibility of TFN membranes. The impact of OH-MoS_2 nanosheets on the physicochemical properties of the TFN membranes was studied and found to significantly change the hydrophilicity, negative charge and surface morphology of the membranes which correlated well with enhanced NF performance. The membranes synthesized were evaluated for pure water flux and salt rejection while organic fouling resistance and organic removal experiments were carried out with feed water containing humic acid (HA) as a hydrophobic synthetic surrogate for NOM.

2. Materials and methods

2.1. Materials and chemicals

Polyethersulfone (PES) ultrafiltration (UF) membrane with MWCO of 50,000 Da was purchased from RisingSun Membrane Technology Co., Ltd., cellulose nitrate membranes with 0.45 μm pore size was purchased from Microanalytix Pty., Ltd., and commercial Trisep XN 45 NF membranes were purchased from Sterlitech. Piperazine (PIP, ≥99%),

Trimesoylchloride (TMC, ≥98%), triethylamine (TEA), camphorsulfonic acid (CSA), sucrose, h-MoS_2 powder (<2 μm, 98%), sodium salt of HA and dialysis tube (MWCO: 3500 kDa) were procured from Sigma Aldrich. N-hexane (≥99%), sodium chloride, sodium sulphate, magnesium sulphate, hydrochloric acid (32%) and sodium hydroxide were supplied by Merck. Other than HA, all chemicals were used as purchased.

2.2. Synthesis of OH-MoS_2 nanosheets

Briefly, bulk h-MoS_2 powder and sucrose were mixed inside a steel bowl in the planetary ball mill (Pulverisette 7, Fritsch) at a weight ratio of 1:50. The mixing was performed under ambient temperature at a rotation speed of 400 rpm for 3 h. The process parameters were chosen based on our previous study and Figure S1 (a) represents the schematic of the synthesis process (Su et al., 2020). Few-layer MoS_2 nanosheets were generated due to the high-impact force and friction force generated with balls and sucrose during ball milling. At termination of the process the samples were dispersed into water, dialysed for a week to remove sucrose and centrifuged. Finally, OH-MoS_2 nanosheets in water were obtained.

2.3. Fabrication of the TFN NF membrane

Fabrication of TFN membranes were based on IP reaction on commercial PES UF support membranes. The membranes were soaked in deionized (DI) water for minimum of 24 h before the fabrication procedure. Then, the membrane was fixed in a plate and frame assembly for the polymerization reaction. The schematic illustration of the membrane synthesis process is shown in Figure S1 (b). First, the aqueous phase containing 2 wt% PIP, 2 wt% CSA, 2 wt% TEA and different amounts of OH-MoS_2 (0.000, 0.002, 0.004, 0.008, 0.010, 0.020 wt%) was allowed to contact the membrane surface for 2 min and then poured away. The membrane surface was rolled with a soft rubber roller to remove visible droplets and uniformly distribute the phase. Next, the organic phase containing 0.1 wt% TMC in n-Hexane was allowed to contact for 1 min. The excess was poured away, and the membrane was washed with n-Hexane. Finally, the membrane was subjected to heat treatment in a digital oven at 70 °C for 2 min followed by washing and storage in DI water for later use. To homogeneously disperse the MoS_2 nanosheets in the aqueous phase, ultrasonication was employed using an ultrasonic cleaner at 100 W for 30 min at room temperature. The membrane samples were named as M0, M1, M2, M3, M4 and M5 for the membranes with OH-MoS_2 content at 0.000, 0.002, 0.004, 0.008, 0.010 and 0.020 wt% respectively. Commercial XN 45 membranes were utilized to benchmark and compare the membrane performance.

2.4. Characterization of OH-MoS_2 nanosheets and TFN membranes

The physicochemical properties of the synthesized OH-MoS_2 nanosheets and membranes were comprehensively evaluated using the following techniques. All the membranes were dried in a desiccator for 24 h prior to characterization.

2.4.1. Field emission-scanning electron microscopy (FE-SEM)

FE-SEM was employed using Supra 55 VP (ZEISS, Germany) to study the morphology of OH-MoS_2 nanosheets, surface and cross-sectional morphologies of membranes. For nanosheets morphology, silicon substrate was cleaned by sonication for 10 min in acetone, ethanol, and water successively, and dried before use. The OH-MoS_2 dispersion was diluted to around 0.01 mg mL^{-1} and dropped on the substrate. After drying at room temperature, the samples were coated with gold before imaging. Surface morphology of membranes were recorded at 5 kV with working distance 10 mm. The membrane samples were coated with gold prior to imaging. For cross-sectional morphologies of membrane, thin strips of membranes were soaked in ethanol for 5 s, rinsed with DI water, freeze-fractured in liquid nitrogen, dried and finally gold coated prior to imaging. Low magnification images were recorded at 3 kV with a working distance of 6 mm while high magnification images were taken at 5 kV with 5 mm working distance. The thickness of the PPA layer was measured at 3 different spots and average values are reported.

2.4.2. Atomic force microscopy (AFM)

The size and thickness of OH-MoS_2 nanosheets as well as membrane surface roughness were examined by AFM using Bruker Multimode 8 operating in non-contact mode at room temperature. For nanosheet morphology study, OH-MoS_2 dispersion was diluted to around 0.001 mg mL^{-1} and dropped on mica substrate. The samples were dried at room temperature before test. The root average arithmetic roughness (R_a), root mean surface roughness (R_q) and root peak to valley distance (R_{max}) were used for analysing membrane surface roughness for a scanning area of 5 μm × 5 μm. To check reproducibility, roughness parameters were measured for 3 random spots on the membrane sample and average values were reported.

2.4.3. Attenuated total reflectance-fourier transform infrared (ATR-FTIR) spectroscopy

Chemical structure and functional groups present on nanosheets, and membranes were studied using ATR-FTIR spectroscopy employing Bruker Vertex 70 FTIR with a scan range from 400 to 4000 cm^{-1} with 64 scans at a resolution of 4 cm^{-1}. FTIR for bulk MoS_2 powder was conducted using KBr pellet method while the FTIR for OH-MoS_2 nanosheet was conducted by vacuum filtering the nanosheet dispersion over a polycarbonate membrane. The FTIR of blank polycarbonate membrane was also included for comparison.

2.4.4. Raman spectroscopy

Raman spectra of membrane were obtained using Renishaw Raman confocal microscope. The membrane samples were cut into 1.0 cm × 1.0 cm before characterization and mounted on glass slide. Excitation was provided by a 514 nm He–Ne laser and a 50 × objective (Olympus) was used for focusing laser beam and collect the signal.

2.4.5. Contact angle (CA) measurements

The membrane surface hydrophilicity was assessed by water CA detected by CAM 101 contact angle/surface tension measuring system (KSV, Finland). The membrane samples were cut into 1.0 cm × 1.0 cm dimensions and attached to a glass slide prior to CA measurements. 3 μL of DI water was placed on to a membrane surface, while static image of the droplet was taken. Attention Theta software was utilized for image analysis and CA computation. To confirm reproducibility, 3 stabilized CA were taken from random spots on the membrane surface and average value were reported.

2.4.6. Streaming potential measurements

Surface charge of the membranes were measured using Surpass Anton Paar electro kinetic analyser (Australia). The membrane samples were cut into two 2.0 cm × 1.0 cm pieces and attached to sample holders which were inserted into a cell with adjustable gap thickness for the measurements. The background electrolyte used was 1 mM NaCl solution and pH was adjusted using 0.1 M NaOH and HCl solutions. To confirm reproducibility, each measurement was conducted four times by changing flow direction within cell and average values were reported.

2.5. Evaluation of TFN NF membranes performance

Permeation, separation, and antifouling performance of the membranes were conducted using a Sterlitech CF042 cross-flow filtration module with an active membrane surface area of 42 cm^2. The membranes were first compacted at 8 bar pressure for 3 h and then pure water flux was measured at 6 bar for 1 h. This was followed with filtration of HA feed solution at 6 bar for 6 h. All the filtration experiments in this study were conducted at ambient room temperature (25 °C). HA feed solution with concentration around 7 mg L^{-1} was prepared using the method mentioned in our previous study mimicking the surface water conditions (Abdikheibari et al., 2018). The conductivity was maintained at 300 ± 10 μS/cm (using 1 M NaCl solution) and pH at 7 ± 0.05 (using 0.1 M HCl or NaOH solution). During each experiment, the feed water was pumped at a constant pressure of 6 bar via HYDRA-CELL pump and water flux was calculated according to Eq. (1):

$$J = \frac{Q}{A \times t} \tag{1}$$

where, J is the membrane flux in (L m^{-2} h^{-1}), Q is the permeate volume (L), A is the membrane surface area (m^2), and t is time in (h). The water permeance of each membrane was calculated according to Eq. (2):

$$WP = \frac{J}{\Delta p} \tag{2}$$

where, WP is the water permeance in (L m^{-2} h^{-1} bar^{-1}) Δp is the pressure difference (bar).

The DOC and UV_{254} rejection were calculated for the permeate and feed collected every hour using a total organic carbon analyser (TOC-L, SHIMADZU Corporation, Japan), and UV spectrophotometer (Spetroquant, Paro 300, Merk), respectively. Salt rejection was analysed using conductivity meter (Thermofisher). The rejection values were calculated according to Eq. (3):

$$R\,(\%) = 1 - \frac{C_p}{C_f} \tag{3}$$

Where, R is the rejection (%), C_f is the solute concentration in feed solution (mg L^{-1} for DOC, cm^{-1} for UV_{254} and μS cm^{-1} for salt rejection) and C_p is the solute concentration in permeate solution (mg L^{-1} for DOC, cm^{-1} for UV_{254} and μS cm^{-1} for salt rejection).

The normalized flux was calculated to study the antifouling performance of membranes using Eq. (4):

$$N_T = \left(\frac{J_T}{J_0}\right) \times 100\% \tag{4}$$

Where, N_T is the normalized flux, J_T is the flux at end of the experiment and J_0 is the initial flux at the start of the experiment.

At the end of 6 h fouling experiments, the fouled membranes were flushed thoroughly with pure water for 20 min. Subsequently, pure water was pumped again into system to collect flux data (F_{re}), to evaluate relative flux recovery ratio (R_{re}) according to Eq. (5):

$$R_{re} = \frac{F_{re}}{F_0} \times 100\% \tag{5}$$

Where, F_0 is initial pure water flux prior to fouling experiments.

Salt rejection experiments were carried with feed water containing 1000 ppm Na_2SO_4, $MgSO_4$ and NaCl respectively. 16 h stability tests were performed for selected membranes to evaluate long term stability performance with Na_2SO_4 feed at 6 bar pressure after compaction at 8 bar for 2 h. The feed and permeate were collected every hour to calculate permeance, salt rejection and permeance decline. All experiments were conducted in triplicate membrane samples to confirm the accuracy and reproducibility of the results and average values are reported for pure water flux, permeance, UV_{254} and DOC rejections, and normalized flux.

3. Results and discussion

3.1. Physical and chemical properties of OH-MoS_2 nanosheets

Several characterization techniques were employed to thoroughly study the physicochemical properties of the synthesized OH-MoS_2 nanosheets. The morphology of nanosheets observed by SEM in Fig. 1(a) exhibited layered structure of OH-MoS_2 of ultrasmall size 60–80 nm in lateral size. The morphology and thickness of OH-MoS_2 nanosheets via AFM revealed the lateral size and thickness of ∼72.0 nm and ∼3.4 nm respectively as shown in Fig. 1(c). The zetasizer data as shown in Figure S2 (a) also supports average nanosheets size to be in the similar range. The thickness of monolayer MoS_2 is 0.62 nm, hence the synthesized OH-MoS_2 nanosheets had a structure within 5–6 layers (Ma et al., 2019; Yang et al., 2020). When compared to other techniques, this unique ball milling procedure was able to achieve ultrasmall lateral size of MoS_2 nanosheets particularly for TFN membrane application (Yang et al., 2020; Li et al., 2019; Zhang et al., 2020a). The ultrasmall size can help in seamless integration of nanosheets into the polyamide matrix and avoid aggregation (Ma et al., 2019). In addition, the zeta potential of nanosheets dispersion was at −42.8 mV at neutral pH indicating very high hydrophilic nature (Su et al., 2020).

The functional groups attached to nanosheets were confirmed by FTIR analysis. FTIR of bulk MoS_2 powder in Figure S2 (b) reveals strong peak at 474.47 cm^{-1} confirming the presence of Mo–S bond. The OH-MoS_2 nanosheets dispersion was vacuum filtered on polycarbonate support membrane and the FTIR graph obtained is included in Fig. 1(b). The peaks at 1640 cm^{-1} and 1450 cm^{-1} are attributed to MoS_2 while the peaks at 1380 cm^{-1} and 931.39 cm^{-1} represents Mo–O and S–S bonds (Chaudhary et al., 2018; Raza et al., 2020; Feng et al., 2015). The broad peak around 3000–3500 cm^{-1} is attributed to symmetric stretching vibration of O–H groups attached to the nanosheets (Raza et al., 2020). The OH functionalization contributes to very high hydrophilicity and extraordinary stability to the nanosheets as confirmed by zeta potential and no visible aggregation was formed in nanosheets dispersion after 6 months as shown in Figure S2 (c) (Su et al., 2020). The hydrophilic properties along with ultrasmall size can enhance the compatibility of nanosheets within PPA layer making it highly suitable nanofillers for TFN membranes (Ma et al., 2019). At the same time the abundant availability of -OH groups can support formation of hydrogen bonds between the nanosheets and hydrated ions and alter the IP reaction enhancing the nanofiltration and antifouling performance while also promoting covalent interactions with the polymer matrix (Xue and Zhang, 2021; Sheng et al., 2021; Ma et al., 2019).

3.2. Characterization of TFN NF membranes

3.2.1. Membrane surface morphology

The surface and cross-sectional morphologies of membranes were studied to investigate the impact of OH-MoS_2 nanosheets on the PPA layer. Figure S3 (a) shows the morphology of the commercial PES ultrafiltration membrane employed in the study. The membrane exhibits porous, smooth, and homogeneous structure. The surface morphology of XN45 membrane as shown in Fig. 2(a) holds a uniformly distributed nodular structure. The control PPA membrane Fig. 2(b) holds a relatively smooth surface with typical bubble-like structures with round protrusions caused due to the fast IP reaction between PIP and TMC (Yang et al., 2020; Yang and Zhang, 2019). The surface morphology of membranes significantly changed on incorporation of OH-MoS_2 nanosheets. As observed in Fig. 2(c)–(f) increasing OH-MoS_2 concentration led to the transition of PPA layer morphology from typical bubble-like structures to crumpled microarchitectures. The transition is ascribed to the change in IP reaction rate on addition of nanosheets (Mallya et al., 2021). At an optimum concentration of 0.010 wt% the surface of the membrane appeared with extensively crumpled and fishnet like structures without formation of any visible defects as shown in Fig. 2(f). In a typical IP reaction between PIP and TMC, PIP from aqueous phase diffuses into the organic phase, which is the rate limiting step controlling the PPA layer formation. The addition of OH-MoS_2 nanosheets can lead to local enrichment of PIP molecules through hydrogen bonding facilitating IP reaction around the nanosheets causing formation of crumpled fishnet like structures (Zhang et al., 2020a). In addition, the hydroxyl groups present on the nanosheets can also interact covalently with TMC affecting the IP reaction (Zhang et al., 2020b). However, on increasing the concentration of nanosheets further to 0.020 wt% dense, smooth and agglomerated microarchitectures with disappearance of crumpled structures was observed as shown in Figure S3 (b). It is well noted that incorporation of nanosheets at higher concentration severely impacted the IP reaction causing localized defects leading to poor separation and antifouling performance (Abdikheibari et al., 2018; Li et al., 2019; Mallya et al., 2021).

Low and high magnification SEM images were utilized to comprehensively study the impact of nanosheets on the inner section of the membranes. Figure S4 (a), (c) and (e) represents the low magnification images of XN45, M0 and M4

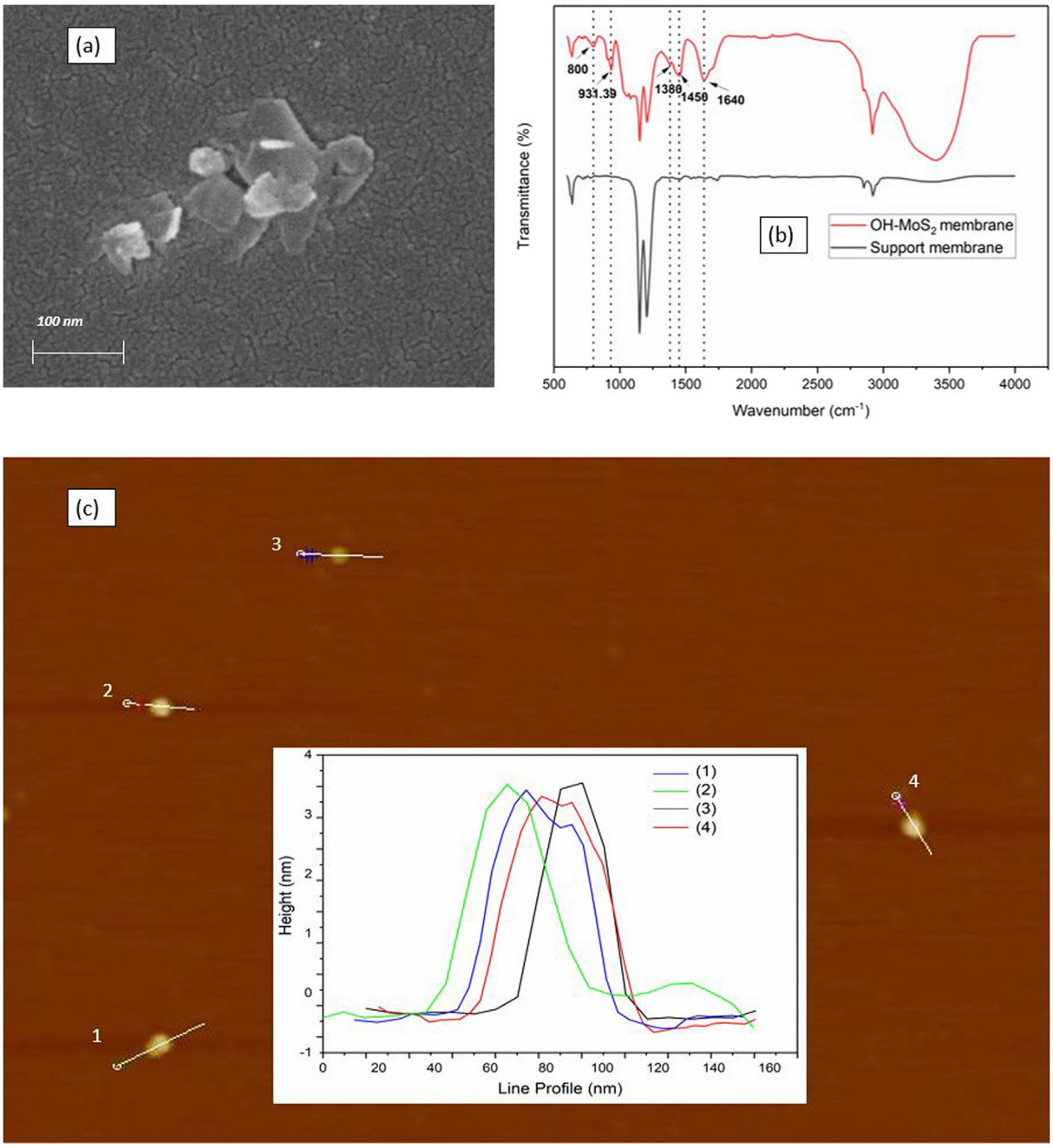

Fig. 1. Characterization results of the OH-MoS_2 nanosheets: (a) SEM images of the OH-MoS_2 nanosheets, (b) FTIR spectrum of OH-MoS_2 nanosheets dispersion vacuum filtered on the support polycarbonate membrane and (c) AFM image and corresponding height profile of OH-MoS_2 nanosheets.

membranes respectively. All the membranes exhibit typical cross-sectional structures with a dense skin layer over porous sponge-like structures. In the case of M4 membrane incorporated with 0.010 wt% OH-MoS_2 nanosheets, the skin layer contains visible nanosheets like structures in the polymer matrix confirming the presence of the nanosheets. Figure S4 (b), (d) and (f) are high magnification images of XN45, M0 and M4 membranes respectively. They exhibit the formation of thin PPA layer over the PES substrate via IP process. The average film thickness of XN45 membrane used in this study was 90.5 nm, while the synthesized control PPA membrane in this study had an average film thickness of 120.6 nm. On incorporation of 0.010 wt% OH-MoS_2 nanosheets, the average thickness of the PPA film slightly increased to 139.96 nm. This was mainly attributed to the promoted IP reaction leading to dense and thick PPA film. In addition, the nanosheets can orient in the vertical directions leading to their interference with upward diffusion of PIP molecules in the organic

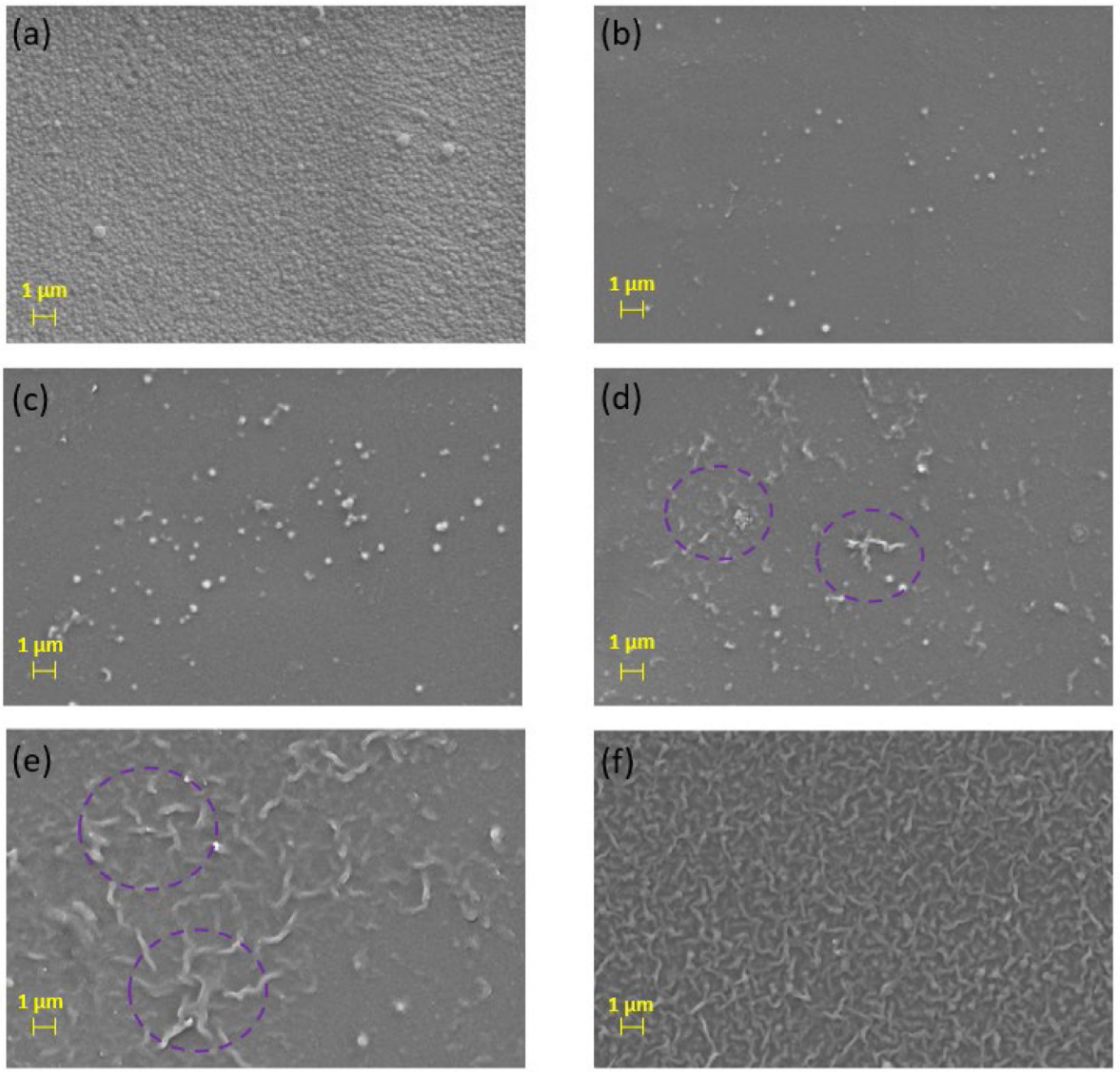

Fig. 2. SEM surface morphologies of (a) XN45, (b) M0, (c) M1, (d) M2, (e) M3, and (f) M4 respectively.

phase and the size of the nanosheets can add onto the PPA film and increase its thickness. The thicker PPA film could not directly translate into increased mass transfer resistance as observed in the pure water flux studies in the following section. The increased film thickness is due to the contribution of PPA film, porous nanofillers and its vertical alignment as well as formation of interfacial voids (Liu et al., 2020). However, PPA layer thickness of the membranes used in this study fall well within the range 70–400 nm usually observed in the literature for nanosheets enabled membranes (Ge et al., 2021; Kang et al., 2019; Yang and Zhang, 2019; Wang et al., 2020).

The membrane surface roughness was measured by AFM, 2D and 3D scan images were displayed in Fig. 3(a)–(c) with scan area 5 µm × 5 µm for the selected membranes M0, M4 and M5 respectively. Table S1 summarizes the measured roughness parameters in terms R_a, R_q and R_{max}. The control membrane synthesized in this study possesses a smooth membrane surface with Rq value of 9.39 nm. Incorporation of 0.010 wt% OH-MoS_2 nanosheets significantly increased the membrane surface roughness Rq value to 20.5 nm. The results are in agreement with SEM images in Fig. 2(f) showing crumpled fishnet like structures on incorporation of 0.010 wt% OH-MoS_2 nanosheets. During IP reaction the diffusion of PIP into organic phase is the rate limiting step. Various additives are incorporated to tailor this phenomenon (Mallya et al., 2021). In our case, the local enrichment of PIP molecules through hydrogen bonding with -OH groups attached on the edges of MoS_2 nanosheets can significantly promote the diffusion of PIP during IP reaction. In addition, the availability of -OH groups on nanosheet structures in different orientations can lead to multiple growth directions during IP reaction

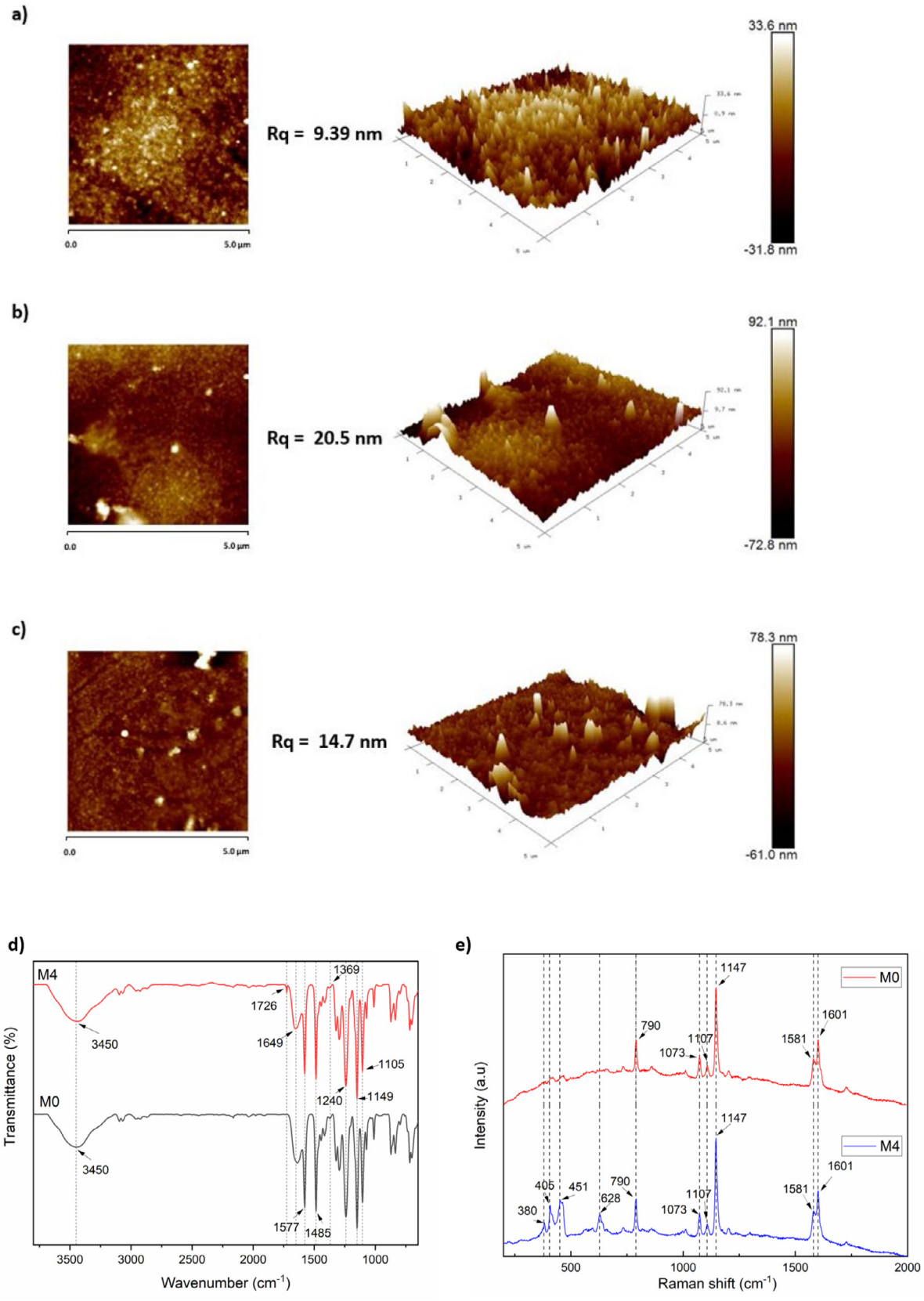

Fig. 3. AFM images of (a) M0, (b) M4, and (c) M5 membranes. (d) ATR-FTIR spectra of M0 and M4 membranes, (e) Raman spectra of M0 and M4 membranes.

giving rise to more protrusions and crumpled structures while leading to thicker skin layer as observed in Fig. 2(f) and Figure S4 (e),(f) (Zhang et al., 2020a; Ma et al., 2019; Xue and Zhang, 2021). However, further increase in the OH-MoS_2 concentration beyond 0.010 wt% resulted in smoother membrane surface with visible agglomeration of the PPA layer as shown in Figure S3 (b) which is undesirable as it would deteriorate the membrane performance.

3.2.2. Chemical compositions of membrane

The chemical composition of the control PPA membrane and 0.010 wt% OH-MoS_2 were investigated using FTIR spectroscopy and Raman spectroscopy. Fig. 3(d) represents the FTIR spectra of the membranes. Both the membranes exhibit peaks for the support PES membrane. The peaks at 1577 and 1485 cm^{-1} are attributed to the C=C aromatic stretching while the doublet at 1321 and 1296 cm^{-1} are from asymmetric stretching of $O = S = O$ of sulfone groups and asymmetric vibration of $C - O - C$ groups. The peaks at 1240, 1149 and 1105 cm^{-1} originate from the aryl ether group, symmetric stretching of $O = S = O$ of sulfone groups and C–O stretching respectively (Abdikheibari et al., 2018; Belfer et al., 2000). The prominent peak around 1649 cm^{-1} belongs to the stretching vibration of C=O of amide I and the peak at 1369 cm^{-1} corresponds to C-N vibrations of the amide groups. These respective peaks confirm the successful formation of PPA layer. In addition, the broad peaks around 3450 cm^{-1} corresponds to the hydroxyl groups formed from hydrolysis of unreacted carboxylic acid groups (Ma et al., 2019). The 0.010 wt% OH-MoS_2 incorporated membrane exhibits a very weak peak around 1726 cm^{-1} corresponding to the formation of polyester groups formed due to the reaction of a fraction of -OH groups attached to nanosheets with unreacted TMC (Ma et al., 2019; Zhang et al., 2020a). This confirms the mechanism of covalent interaction of OH-MoS_2 nanosheets with the PPA layer.

Fig. 3 (e) shows the Raman spectra of control PPA and 0.010 wt% OH-MoS_2 incorporated membranes. The peaks located around 790, 1073, 1107, 1147, 1589 and 1600 cm^{-1} can be associated with the polyamide functional groups (Jafarinejad et al., 2019). The peaks at 790, 1581 and 1601 cm^{-1} are due to the asymmetric C-N-C stretching of tertiary amide groups, aromatic in-plane bending vibration and aromatic amide groups respectively (Jafarinejad et al., 2019; Lamsal et al., 2012). The bands at 1147, 1107 and 1073 cm^{-1} are associated with C-N stretching vibrations of piperazine rings and amide groups (Lamsal et al., 2012). When compared to control PPA membrane, OH-MoS_2 incorporated membrane observed unique peaks at 380, 405 and 451 cm^{-1} which confirms the embedding of OH-MoS_2 nanosheets into the PPA layer (Li et al., 2019). The peaks at 380 cm^{-1} and 406 cm^{-1} corresponds to the in-plane vibration of Mo and S atoms and the out-of-plane vibration of S atoms respectively (Wu et al., 2018). The peaks at 451 cm^{-1} and 463 cm^{-1} are associated with Mo–O, while peak 625 cm^{-1} can be corresponded to C-S respectively validating the interaction mechanisms of OH-MoS_2 nanosheets with the PPA layer (Yang et al., 2018; Cotton and Feng, 1998).

3.2.3. Membrane surface hydrophilicity and electronegativity

CA measurements were conducted to assess the membrane surface hydrophilicity of commercial, prepared membranes and reported in Figure S5 (a). The higher CA represents low hydrophilic properties of the membrane. The highest CA at 62° was recorded for PES support membrane due to its inherent hydrophobic nature as observed in several literatures (Khosravi et al., 2022; Mehrjo et al., 2021). On synthesis of PPA selective layer over the membrane the hydrophilicity increased as the CA reduced to 38.2°. This was attributed to the availability of abundant carboxylic groups on the membrane surface of PPA layer (Abdikheibari et al., 2018). The commercial XN 45 membrane recorded a smooth and hydrophilic surface with CA at 42.5°. Addition of OH-MoS_2 nanosheets resulted in decreasing the CA of TFN membranes. Incorporation of 0.010 wt% OH-MoS_2 nanosheets reduced the CA by 30.89% from 38.2° to 26.4° when compared to control PPA membrane. This was attributed to the highly hydrophilic nature of the OH-MoS_2 nanosheets with a zeta potential value of −42.5 mV at neutral pH (Su et al., 2020). The facile functionalization provides -OH functional groups to the nanosheets improving its ability to absorb water molecules through hydrogen bonding and improve the hydrophilic nature of the membrane surface (Ashfaq et al., 2020; Kang et al., 2019). This enhanced hydrophilicity of membrane and can mitigate organic fouling (Selvan et al., 2022). However, increasing the concentration to further 0.020 wt% resulted in an increase in CA which can be attributed to the reduction in free carboxyl groups on the membrane surface as they can react with -OH groups of the nanosheets to form ester bonds (Ma et al., 2019; Zhang et al., 2020a). In addition, at 0.020 wt%, the membrane surface tends to be smoother as observed in Fig. 3(c).

The surface charge of the membrane greatly influences its permeance, salt rejection and antifouling performance (Yang et al., 2020). At neutral pH NF membranes hold a negatively charged surface due to disassociation of the free carboxylic acid groups (Abdikheibari et al., 2018). As observed in the Figure S5 (b) membrane M0 and M5 synthesized in this study show a zeta potential range (−40 mV to −60 mV) commonly observed for PIP-TMC membranes (Ma et al., 2019; Kang et al., 2019; Yang et al., 2020). Incorporation of OH-MoS_2 nanosheets led to enhancement in the electronegativity of NF membranes. 0.010 wt% OH-MoS_2 nanosheets incorporated TFN membrane exhibited enhanced zeta potential from −42.56 mV to −56.85 mV at neutral pH when compared to the control PPA membrane. This trend was mainly attributed to the electronegative nature endowed by OH-MoS_2 nanosheets. The results infer that the incorporation of OH-MoS_2 nanosheets enhanced the electronegativity properties of the TFN membranes enhancing the repulsion to negatively charged salt ions and hydrophobic NOM moieties improving the selectivity and antifouling performance. The surface negative charge was boosted mainly due to the electronegative nature of OH-MoS_2 nanosheets and the attached hydroxyl groups (Ashfaq et al., 2020; Kang et al., 2019; Yang et al., 2020). Above 0.010 wt% the surface negative charge lowered, this could be attributed to the aggregation and uneven distribution of the nanosheets. The PPA layer became more denser

as observed in SEM image shown in Figure S3 (b) which could be attributed to the formation of Mo–O covalent bonds (Fig. 3(e)) that can promote further formation of amide bonds during IP reaction (Yang et al., 2020). This along with the formation of ester bonds can significantly reduce the free carboxylic group thereby reducing surface charge and hydrophilicity of membranes at higher content of OH-MoS_2 nanosheets (Ma et al., 2019).

3.3. Filtration performance

Pure water flux, salt rejection, NOM rejection, fouling resistance and stability of the membranes were studied using a lab scale cross flow filtration setup to evaluate the performance of OH-MoS_2 incorporated membranes and benchmark with control and commercial membrane.

3.3.1. Pure water flux and Na_2SO_4 rejection

The pure water flux of the membranes increased with increase in OH-MoS_2 concentration as shown in Fig. 4(a). At an optimum concentration of 0.010 wt% the pure water flux of the TFN membrane showed highest value at 84.14 L m^{-2} h^{-1} when compared to control membrane the flux was enhanced by 45.17% from 57.96 L m^{-2} h^{-1}. 0.010 wt% OH-MoS_2 nanosheets incorporated TFN membrane exhibited higher pure water flux than the commercial XN45 membrane supporting its practical application. The trade-off between permeance and salt rejection was bridged as the OH-MoS_2 nanosheets was incorporated in TFN membranes. The 0.010 wt% OH-MoS_2 TFN membrane showed enhanced rejection of Na_2SO_4 at 96.67% when compared to control PPA membrane at 91.38% as shown in Fig. 4(b). The improved membrane performance can be linked to the following several reasons: (1) increased hydrophilicity of the OH-MoS_2-TFN membranes can be attributed to the hydrophilic sites on OH-MoS_2 nanosheets capable for forming hydrogen bonds with water molecules favouring swift transport of water increasing the membrane flux (Yang et al., 2020). This was confirmed by CA measurements with decreased CA on incorporation of OH-MoS_2 nanosheets. (2) In addition, the OH-MoS_2 nanosheets promotes the IP reaction through hydrogen bonding creating crumpled and fishnet structures as shown in Fig. 2(f), enhancing formation of nanovoids and micropores selectively allowing water molecules to pass through (Zhang et al., 2020a; Ma et al., 2019). (3) The interfacial voids presenting in the adjacent OH-MoS_2 nanosheet layers can also act as alternate transport pathways for water molecules increasing the water flux. The salt rejection test results revealed enhanced rejection on addition of 0.010 wt% OH-MoS_2 nanosheets. The rejection of Na_2SO_4 increased from 91.38% to 96.67%, $MgSO_4$ increased from 83.16% to 92.18% while tremendous increase in NaCl rejection from 32.56% to 64.56% was recorded when compared to control membrane. The salt rejection was maintained high mainly due to the enhanced electronegativity on incorporation of OH-MoS_2 nanosheets and also can be attributed to the partial coverage of nanopores by nanosheets (Yang et al., 2020; Zhang et al., 2020a). The salt rejection and flux were in range reported for TFN membranes in literature while performing better than GO, BN and g-C_3N_4 incorporated NF membrane as summarized in Table 1. When compared to studies involving MoS_2 nanosheets modified TFN membranes, the 0.010 wt% OH-MoS_2 incorporated membrane showed very good performance in terms of pure water flux and salt rejection as shown in Table 1.

In addition, 16 h stability tests with 1000 ppm Na_2SO_4 at 6 bar pressure revealed superior performance of OH-MoS_2 incorporated TFN membrane (Figure S6). The normalized permeance of TFN membrane at the end of 16 h was 93.65% compared to control membrane at 74% as shown in Figure S6. This also confirmed that incorporation of OH-MoS_2 nanosheets enhanced permeance and the mechanical stability of NF membrane as well as maintained stable filtration performance with Na_2SO_4 rejection >96.5%.

3.3.2. Fouling resistance performance and NOM removal

Fig. 4 (c) and (d) show the normalized flux trend of NF membranes during 6-hour fouling experiments. All the membranes subjected to this test exhibit flux decline with 0.010 wt% OH-MoS_2 nanosheets incorporated membrane exhibiting high normalized flux retained with 96.92% when compared to control PPA at 91.22% and commercial XN45 membrane at 92.7%. The OH-MoS_2 nanosheets rendered the membrane with higher hydrophilicity as observed by CA measurements resulting in formation of water hydration layer over the membrane surface. This hydrophilic layer helps in preventing the deposition of hydrophobic organic foulants on the membrane surface (Yang et al., 2020; Ma et al., 2019; Li et al., 2019). In addition, the AFM results shown in Fig. 3(b) reveal the increased surface roughness of 0.010 wt% OH-MoS_2 incorporated membrane. This increased surface roughness can enhance the surface area available for filtration promoting development of larger water hydration layer resulting in enhanced fouling resistance (Wang et al., 2020). The surface negative charge was also enhanced on incorporation of OH-MoS_2 nanosheets until the optimum concentration of 0.010 wt%. Due to this electrostatic repulsion between negatively charged membrane surface and hydrophobic organic foulants was increased resulting in reduced deposition of organic foulants as well as the foulants were easily removed by flushing with water. Table S3 summarizes the data on flux and relative flux recovery ratio of selected membranes. It was observed that 0.010 wt % OH-MoS_2 TFN membrane exhibited lowest flux decline rate with 3.08% and highest flux recovery ratio with 98.88% due to its hydrophilic nature. However, as the concentration of OH-MoS_2 nanosheets was increased to 0.020 wt% the membrane negative charge reduced significantly due to unavailability of free carboxylic and the CA was increased indicating less hydrophilicity with the membrane surface becoming more smoother as observed in AFM results shown in Fig. 3(c) (Zhang et al., 2020a).

Table 1
Comparison of the performance characteristics of prepared membranes with other 2D enabled TFN membranes.

Entry	Nanosheet type	Average size (S) and thickness (T)	Optimum concentration in (x) phase	Pure water permeance of control membrane (L m^{-2} $h^{-1}bar^{-1}$)	Pure water permeance of TFN membrane (L m^{-2} $h^{-1}bar^{-1}$)	Performance enhancement (%)	Na_2SO_4 rejection (%)	Ref
1	OH-MoS_2	S = ~72 nm, T = ~3.4 nm	0.010 wt % (A)	9.66	14.023	45.17	96.67	This work
2	MoS_2	S = 200 – 600 nm, T = 3 nm	0.010 wt/v% (O)	3.4	7.8	129.41	94.40	Yang and Zhang (2019)
3	TA-MoS_2,	S = 37.41 nm, T = 1.35 nm	0.0205 wt% (A)	13.67	17	24.36	98.50	Ma et al. (2019)
4	TA-Fe^{3+}-MoS_2	S = 500 – 1500 nm, T = 5 – 6 nm	0.010 wt% (A)	4.9	7.6	55.10	96.30	Zhang et al. (2020a)
5	O-MoS_2	S = 100 – 500 nm, T = 1.8 – 5 nm	0.010 wt/v% (O)	3.11	7.91	154.34	97.9	Yang et al. (2020)
6	$BN(NH_2)$, Ball milling	S = 100 nm, T = 1.5 nm	0.004 wt% (A)	12.92	13.88	7.43	68.93	Abdikheibari et al. (2018)
7	PDA-MoS_2	–	0.010 wt% (A)	4.6	6.7	45.65	98.20	Xie et al. (2022)
8	SGO	–	0.3 wt% (A)	1.27	2.37	87.3	96.45	Kang et al. (2019)
9	g-C_3N_4	–	0.0025 wt% (A)	10.45	18.8	79.90	84	Chen et al. (2016)

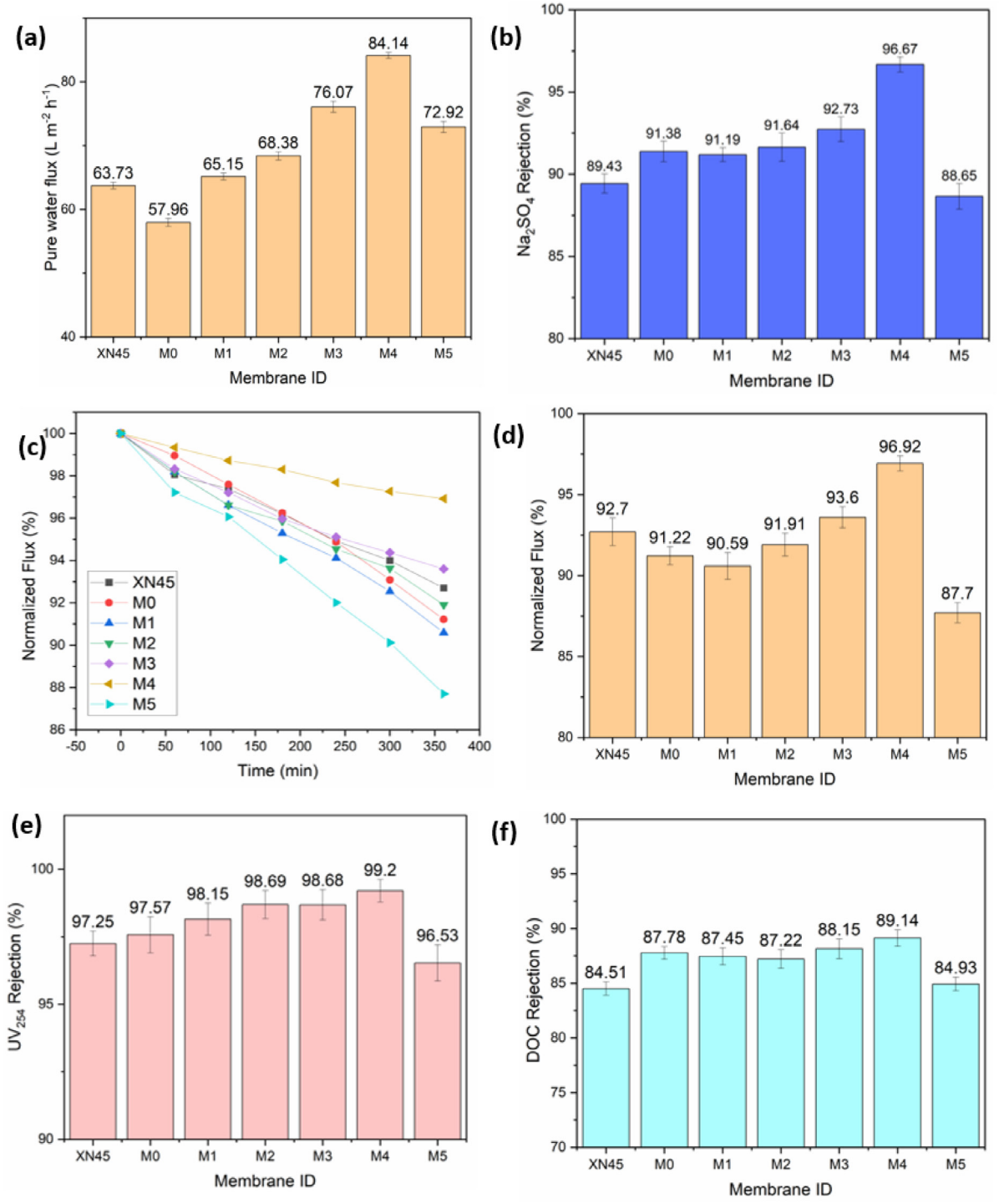

Fig. 4. Nanofiltration, fouling resistance and organic removal performance of membranes evaluated in this study. (a) Pure water flux (b) Na_2SO_4 rejection (c) Normalized flux trend for fouling experiments (d) Normalized flux at the end of 6-hour filtration experiment (e) UV_{254} rejection (f) DOC rejection.

In terms of NOM removal performance, all the membranes in the study exhibited very high UV_{254} removal above 96.5% owing to the negative surface charge of the membranes as shown in Fig. 4(e). DOC rejection values as shown in Fig. 4(f) were maintained above 84% for membranes employed in this study. DOC rejection of commercial XN45, control PPA and

Table 2
Comparison of NOM removal performance for surface water treatment with OH-MoS_2 incorporated membrane with commercial and BN incorporated membranes.

Membrane ID	NOM surrogate	Feed DOC concentration (mg/L)	DOC removal (%)	UV 254 removal (%)	Ref
M4	HA	7.2	89.14	99.20	This work
M0	HA	7.2	87.78	97.57	This work
XN45	HA	7.2	84.51	97.25	This work
PPA-BN-4	HA	6.2	86.56	97.91	Abdikheibari et al. (2018)
NF270	HA	2	n/a	99.40	Song et al. (2011)
Dual modified PPA-BN membrane	Surface water	6	89.00	95.00	Abdikheibari et al. (2020)

0.010 wt% OH-MoS_2 nanosheets incorporated membranes were at 84.51%, 87.78% and 89.14% respectively. The higher DOC rejection of TFN membrane was mainly attributed to the enhanced hydrophilicity and electronegativity imparted by the hydrophilic OH-MoS_2 nanosheets. The optimized membranes exhibited 45.17% increase in pure water flux while maintaining a better performance in terms of organic removal and fouling mitigation. Table 2 presents the comparison of NOM removal performance in terms of DOC and UV_{254} for OH-MoS_2 incorporated membrane in this study with commercial and BN incorporated membranes. The OH-MoS_2 nanosheets incorporated membrane performed superior with very high rejection of DOC and UV_{254}. However, 0.020 wt% OH-MoS_2 incorporated membrane performance indicated lower DOC removal at 84.93% (Fig. 4(f)). This was mainly attributed to the lower hydrophilic nature and electronegativity of the TFN membrane. In addition, the aggregation of nanosheets could lead to formation of unselective defects which allows the transport of organic molecules (Mallya et al., 2021).

The fouling resistance performance of 0.010 wt% OH-MoS_2 nanosheets incorporated membrane was compared with other 2D nanosheets enabled TFN membranes and is summarized in Table S2. The optimized TFN membrane synthesized in this study exhibited very good fouling resistance performance for treatment of surface water containing hydrophobic NOM. The fouling resistance was similar to the BN incorporated TFN membrane however, the higher flux, enhanced salt and NOM rejection make it a better candidate among other 2D nanosheets enabled TFN membranes. In particular, BN incorporated TFN membrane was reported to have low salt rejection of 68.93%, 61.18% and 12.97% for Na_2SO_4, $MgSO_4$ and NaCl respectively (Abdikheibari et al., 2018). In comparison to GO, BN and g-C_3N_4 incorporated TFN membranes, OH-MoS_2 incorporated membranes exhibited superior performance in organic fouling, organic removal, water flux and salt rejection as summarized in Tables 1 and 2, and S2 as well good stability suggesting opportunities for surface water treatment.

4. Conclusions

Novel TFN NF membranes incorporated with functionalized OH-MoS_2 nanosheets (0.000–0.0200 wt%) were synthesized via a simple interfacial polymerization reaction for the removal of HA from water. The few-layer OH-MoS_2 nanosheets synthesized using sugar assisted mechanochemical exfoliation via ball milling endowed the TFN membrane with higher hydrophilicity, negative charge, surface roughness and modified PPA structure to more crumpled fishnet-like microstructures from typical nodular structure. At an optimum concentration of 0.010 wt% OH-MoS_2 nanosheets, the TFN membrane outperformed control and commercial membranes in terms of pure water flux, salt rejection, NOM removal and fouling resistance. The optimized TFN membrane bridged the trade-off between flux and salt rejection with 45.17% increase in flux from 57.96 to 84.14 L m^{-2} h^{-1} with higher salt rejection maintained at 96.67% for Na_2SO_4. The optimized TFN membrane exhibited enhanced fouling resistant behaviour by maintaining 96.92% of the normalized flux during 6 h filtration experiments with HA solution compared to 91.22% for the control PPA membrane. When compared to commercial and other TFN membranes in literature, OH-MoS_2 nanosheets incorporated TFN membrane synthesized in this study performed better in removing NOM surrogate from water while maintaining very high pure water flux, salt rejection and stability. This research supports the successful membrane modification strategy via incorporation of functionalized OH-MoS_2 nanosheets to synthesize novel next-generation fouling resistant membranes which can be employed for various applications in water treatment and other fields in the future. Also, further studies should evaluate long term fouling experiments with multiple cleaning/fouling cycles and antibacterial performance of the TFN membranes. OH-MoS_2 nanosheets can be further utilized to surface engineering fouling resistant membranes by incorporating them as interlayer between the support and PPA film or can be decorated over already formed PPA film.

CRediT authorship contribution statement

Deepak Surendhra Mallya: Conceptualization, Methodology, Visualization, Writing – original draft. **Guoliang Yang:** Visualization, Writing – review & editing. **Weiwei Lei:** Supervision, Writing – review & editing. **Shobha Muthukumaran:** Supervision, Writing – review & editing. **Kanagaratnam Baskaran:** Supervision, Writing – review & editing.

Declaration of competing interest

The authors declare that they have no known competing financial interests or personal relationships that could have appeared to influence the work reported in this paper.

Acknowledgements

The authors gratefully acknowledge Dr. Yuyu Su for guidance on synthesis of nanosheets, Ken Aldren Usman for his kind advice on AFM analysis and Dr. Ludovic F Dumee for his advice on scientific writing. Mr. Mallya and Mr. Yang acknowledges Deakin University for their PhD scholarship. Dr. Weiwei Lei acknowledges ARC for Discovery Program (DP190103290) and Future Fellowship (FT210100804).

Appendix A. Supplementary data

Supplementary material related to this article can be found online at https://doi.org/10.1016/j.eti.2022.102719.

References

Abdikheibari, S., Dumée, L.F., Jegatheesan, V., Mustafa, Z., Le-Clech, P., Lei, W., Baskaran, K., 2020. Natural organic matter removal and fouling resistance properties of a boron nitride nanosheet-functionalized thin film nanocomposite membrane and its impact on permeate chlorine demand. J. Water Process. Eng. 34, 101160.

Abdikheibari, S., Lei, W., Dumée, L.F., Milne, N., Baskaran, K., 2018. Thin film nanocomposite nanofiltration membranes from amine functionalized-boron nitride/polypiperazine amide with enhanced flux and fouling resistance. J. Mater. Chem. A 6, 12066–12081.

Ahmadi, M., Zabihi, O., Yadav, R., Ferdowsi, M.R.G., Naebe, M., 2021. The reinforcing role of 2D graphene analogue MoS2 nanosheets in multiscale carbon fibre composites: Improvement of interfacial adhesion. Compos. Sci. Technol. 207, 108717.

Alosaimi, E.H., Hassan, H.M., Alsohaimi, I.H., Chen, Q., Melhi, S., Younes, A.A, El-Shwiniy, W.H, 2022. Fabrication of sulfonated polyethersulfone ultrafiltration membranes with an excellent antifouling performance by impregnating with polysulfopropyl acrylate coated ZnO nanoparticles. Environ. Technol. Innov. 25, 102210.

Ashfaq, M.Y, Al-Ghouti, M.A, Zouari, N, 2020. Functionalization of reverse osmosis membrane with graphene oxide to reduce both membrane scaling and biofouling. Carbon 166, 374–387.

Belfer, S., Fainchtain, R., Purinson, Y., Kedem, O., 2000. Surface characterization by FTIR-ATR spectroscopy of polyethersulfone membranes-unmodified, modified and protein fouled. J. Membr. Sci. 172, 113–124.

Chaudhary, N., Khanuja, M., Islam, S.S., 2018. Hydrothermal synthesis of MoS2 nanosheets for multiple wavelength optical sensing applications. Sensors Actuators A 277, 190–198.

Chen, J., Li, Z., Wang, C., Wu, H., Liu, G., 2016. Synthesis and characterization of gC 3 N 4 nanosheet modified polyamide nanofiltration membranes with good permeation and antifouling properties. RSC Adv. 6, 112148-112157.

Cotton, F.A., Feng, X., 1998. Density functional theory study of transition-metal compounds containing metal-metal bonds. 2. Molecular structures and vibrational spectra of dinuclear tetracarboxylate compounds of molybdenum and rhodium. J. Am. Chem. Soc. 120, 3387–3397.

Du, Y., Pramanik, B.K., Zhang, Y., Dumée, L., Jegatheesan, V., 2022. Recent advances in the theory and application of nanofiltration: a review. Curr. Pollut. Rep. 8, 51–80.

Feng, W., Chen, L., Qin, M., Zhou, X., Zhang, Q., Miao, Y., Qiu, K., Zhang, Y., He, C., 2015. Flower-like PEGylated MoS2 nanoflakes for near-infrared photothermal cancer therapy. Sci. Rep. 5, 17422.

Ge, M., Wang, X., Wu, S., Long, Y., Yang, Y., Zhang, J., 2021. Highly antifouling and chlorine resistance polyamide reverse osmosis membranes with g-C3N4 nanosheets as nanofiller. Sep. Purif. Technol. 258, 117980.

Gupta, A., Sakthivel, T., Seal, S., 2015. Recent development in 2D materials beyond graphene. Prog. Mater. Sci. 73, 44–126.

Jafarinejad, S., Park, H., Mayton, H., Walker, S.L., Jinag, S.C., 2019. Concentrating ammonium in wastewater by forward osmosis using a surface modified nanofiltration membrane. Environ. Sci.: Water Res. Technol. 5, 246–255.

Kang, Y., Obaid, M., Jang, J., Kim, I.S., 2019. Sulfonated graphene oxide incorporated thin film nanocomposite nanofiltration membrane to enhance permeation and antifouling properties. Desalination 470, 114125.

Khosravi, M.J., Hosseini, S.M., Vatanpour, V., 2022. Performance improvement of PES membrane decorated by Mil-125(Ti)/chitosan nanocomposite for removal of organic pollutants and heavy metal. Chemosphere 290, 133335.

Lamsal, R., Harroun, S.G., Brosseau, C.L., Gagnon, G.A., 2012. Use of surface enhanced Raman spectroscopy for studying fouling on nanofiltration membrane. Sep. Purif. Technol. 96, 7–11.

Li, Y., Yang, S., Zhang, K., Van der Bruggen, B., 2019. Thin film nanocomposite reverse osmosis membrane modified by two dimensional laminar MoS2 with improved desalination performance and fouling-resistant characteristics. Desalination 454, 48–58.

Lim, S., Akther, N., Bae, T.-H., Phuntsho, S., Merenda, A., Dumée, L.F., Shon, H.K., 2020. Covalent organic framework incorporated outer-selective hollow fiber thin-film nanocomposite membranes for osmotically driven desalination. Desalination 485, 114461.

Liu, Y., Wang, X., Gao, X., Zheng, J., Wang, J., Volodin, A., Xie, Y.F., Huang, X., Van der Bruggen, B., Zhu, J., 2020. High-performance thin film nanocomposite membranes enabled by nanomaterials with different dimensions for nanofiltration. J. Membr. Sci. 596, 117717.

Ma, M.-Q., Zhang, C., Zhu, C.-Y., Huang, S., Yang, J., Xu, Z.-K., 2019. Nanocomposite membranes embedded with functionalized MoS2 nanosheets for enhanced interfacial compatibility and nanofiltration performance. J. Membr. Sci. 591, 117316.

Mallya, D.S., Dumee, L.F., Muthukumaran, S., Lei, W.W., Baskaran, K., 2021. 2D Nanosheet enabled thin film nanocomposite membranes for freshwater production - a review. Mater. Adv. 2, 3519–3537.

Mansourpanah, Y., Ghanbari, A., Yazdani, H., Mohammadi, A.G., Rahimpour, A., 2021. Silver-polyamidoamine/graphene oxide thin film nanofiltration membrane with improved antifouling and antibacterial properties for water purification and desalination. Desalination 511, 115109.

Mehrjo, F., Pourkhabbaz, A., Shahbazi, A., 2021. PMO Synthesized and functionalized by p-phenylenediamine as new nanofiller in PES-nanofiltration membrane matrix for efficient treatment of organic dye, heavy metal, and salts from wastewater. Chemosphere 263, 128088.

Metsämuuronen, S., Sillanpää, M., Bhatnagar, A., Mänttäri, M., 2014. Natural organic matter removal from drinking water by membrane technology. Sep. Purif. Rev. 43, 1–61.

Moradi, G., Heydari, R., Zinadini, S., Rahimi, M., Gholami, F., 2021. High-performance nanofiltration membranes consisting of the new functionalized mesoporous for enhanced antifouling attributes and simultaneous removal of salts, dyes and heavy metals. Environ. Technol. Innov. 24, 101929.

Pichardo-Romero, D., Garcia-Arce, Z.P., Zavala-Ramírez, A., Castro-Muñoz, R., 2020. Current advances in biofouling mitigation in membranes for water treatment: An overview. Processes 8, 182.
Raza, A., Ikram, M., Aqeel, M., Imran, M., Ul-Hamid, A., Riaz, K.N., Ali, S., 2020. Enhanced industrial dye degradation using co doped in chemically exfoliated MoS2 nanosheets. Appl. Nanosci. 10, 1535–1544.
Selvan, B.K., Thiyagarajan, K., Das, S., Jaya, N., Jabasingh, S.A., Saravanan, P., Rajasimman, M., Vasseghian, Y., 2022. Synthesis and characterization of nano zerovalent iron-kaolin clay (nZVI-Kaol) composite polyethersulfone (PES) membrane for the efficacious as2o3 removal from potable water samples. Chemosphere 288, 132405.
Shahabi, S.S., Azizi, N., Vatanpour, V., 2019. Synthesis and characterization of novel g-C3N4 modified thin film nanocomposite reverse osmosis membranes to enhance desalination performance and fouling resistance. Sep. Purif. Technol. 215, 430–440.
Sheng, F., Wu, B., Li, X., Xu, T., Shehzad, M.A., Wang, X., Ge, L., Wang, H., Xu, T., 2021. Efficient ion sieving in covalent organic framework membranes with sub-2-nanometer channels. Adv. Mater. 33, 2104404.
Shurvell, T., Farago, L., Jegatheesan, V., Shu, L., 2015. Removal of natural organic matter though membrane filtration and subsequent effect on disinfectant decay. Desalin. Water Treat. 54, 881–889.
Song, H., Shao, J., He, Y., Hou, J., Chao, W., 2011. Natural organic matter removal and flux decline with charged ultrafiltration and nanofiltration membranes. J. Membr. Sci. 376, 179–187.
Su, Y., Liu, D., Yang, G., Han, Q., Qian, Y., Liu, Y., Wang, L., Razal, J.M., Lei, W., 2020. Transition metal dichalcogenide (TMD) membranes with ultrasmall nanosheets for ultrafast molecule separation. ACS Appl. Mater. Interfaces 12, 45453–45459.
USEPA, 2006. Vol. Federal Reg. 71. pp. 387–493.
Wang, X.Y., Li, Q.Q., Zhang, J.F., Huang, H.M., Wu, S.Y., Yang, Y., 2020. Novel thin-film reverse osmosis membrane with mxene ti3c2tx embedded in polyamide to enhance the water flux, anti-fouling and chlorine resistance for water desalination. J. Membr. Sci. 603, 12.
Wen, Y., Chen, Y.Q., Wu, Z.C., Liu, M.X., Wang, Z.W., 2019. Thin-film nanocomposite membranes incorporated with water stable metal–organic framework CuBTTri for mitigating biofouling. J. Membr. Sci. 582, 289–297.
WHO, 2011. Guidelines for drinking-water quality. WHO Chronicle, 38. pp. 104–108.
Wu, P.-R., Kong, Y.-C., Ma, Z.-S., Ge, T., Feng, Y.-M., Liu, Z., Cheng, Z.-L., 2018. Preparation and tribological properties of novel zinc borate/MoS2 nanocomposites in grease. J. Alloys Compd. 740, 823–829.
Wu, Y.P., Xue, Y., Qin, S., Liu, D., Wang, X.B., Hu, X., Li, J.L., Wang, X.G., Bando, Y., Golberg, D., Chen, Y., Gogotsi, Y., Lei, W.W., 2017. Bn nanosheet/polymer films with highly anisotropic thermal conductivity for thermal management applications. Acs Appl. Mater. Interfaces 9, 43163–43170.
Xie, F., Li, W.-X., Gong, X.-Y., Taymazov, D., Ding, H.-Z., Zhang, H., Ma, X.-H., Xu, Z.-L., 2022. MoS2 @pda thin-film nanocomposite nanofiltration membrane for simultaneously improved permeability and selectivity. J. Environ. Chem. Eng. 10, 107697.
Xue, Q., Zhang, K., 2021. The preparation of high-performance and stable mxene nanofiltration membranes with mxene embedded in the organic phase. Membranes 12 (2).
Yang, S., Jiang, Q., Zhang, K., 2020. Few-layers 2D O-MoS2 TFN nanofiltration membranes for future desalination. J. Membr. Sci. 118052.
Yang, Y., Pu, H., Di, J., Zhang, S., Hu, J., Zang, Y., Gao, C., Chen, C., 2018. Influences of temperature gradient and distance on the morphologies of MoS2 domains. AIP Adv. 8, 085218.
Yang, S., Zhang, K., 2019. Few-layers MoS2 nanosheets modified thin film composite nanofiltration membranes with improved separation performance. J. Membr. Sci. 117526.
Zhang, H., Gong, X.-Y., Li, W.-X., Ma, X.-H., Tang, C.Y., Xu, Z.-L., 2020a. Thin-film nanocomposite membranes containing tannic acid-Fe3+ modified MoS2 nanosheets with enhanced nanofiltration performance. J. Membr. Sci. 118605.
Zhang, Y., Li, X., Wang, Z., Wang, J., 2022. A novel method of fabricating anti-biofouling nanofiltration membrane with almost no potential to induce antimicrobial resistance in bacteria. Sep. Purif. Technol. 120710.
Zhang, Y., Ruan, H., Guo, C., Liao, J., Shen, J., Gao, C., 2020b. Thin-film nanocomposite reverse osmosis membranes with enhanced antibacterial resistance by incorporating p-aminophenol-modified graphene oxide. Sep. Purif. Technol. 234, 116017.
Zhao, S., Liao, Z., Fane, A., Li, J., Tang, C., Zheng, C., Lin, J., Kong, L., 2021. Engineering antifouling reverse osmosis membranes: A review. Desalination 499, 114857.